International Journal of Mechanical and Electrical Engineering
ISSN: 3005-9615 (Print), ISSN: 3005-7132 (Online) | Volume 8, Number 1, Year 2026
DOI: https://doi.org/10.62051/ijmee.v8n1.01
Journal homepage: https://wepub.org/index.php/IJMEE/index

Dynamic and Static Analysis and Optimization Design of the Crossbeam in a Fixed-Gantry Machining Center

Yan Feng *, Bo Huang, Wenke Du

Sichuan University of Science & Engineering, Yibin, Sichuan, China
* Corresponding Author: Yan Feng (Email: feng165329@163.com)

ABSTRACT

In this study, to enhance the overall performance of a gantry machining center's crossbeam, static analysis identified critical load conditions (cutting forces, self-weight, and component loads). Dynamic analysis employed Yoshimura's method to establish joint dynamics models, obtaining modal parameters (natural frequencies, mode shapes, and vibration amplitudes). A hybrid optimization approach combining topology optimization and bionic design was implemented: topology optimization first determined optimal material distribution, followed by bio-inspired rib layout refinement inspired by turtle shell morphology. This methodology achieved balanced static-dynamic performance with lightweight design, integrating computational mechanics and biological structural advantages.

KEYWORDS

Bionic Design; Crossbeam; Dynamic and Static Characteristics; Gantry Machining Center; Topology Optimization.

1. INTRODUCTION

Gantry-type machining centers represent a class of large-scale precision machine tools characterized by high-precision machining capability and processing efficiency, featuring an extended worktable, high load-bearing capacity, and multi-axis coordinated machining functionality [1]. Contemporary machine tool research predominantly focuses on gantry-type machining centers, with particular emphasis on the static-dynamic characteristics of these systems and their core structural components.

Ahmed et al. [2] applied a finite element simulation method to analyze the effect of tool geometry on cutting forces and tool temperatures during tool steel ball end milling (AISI H13). Experiments using single and multi-objective optimal geometries were conducted to validate the finite element analysis. Both finite element and experimental results are in agreement with an error limit of 5%.Niu Peng et al. [3] conducted multi-objective topological optimization of the column's stiffener arrangement using Abaqus software. Subsequent stiffener configuration modifications demonstrated through comparative finite element analysis: 10.09% mass reduction, 5% decrease in maximum displacement, and enhanced fundamental frequency. Li et al. [4] used a finite element model (FEM) to analyze the modal frequencies of the beam and a neural network algorithm to further optimize the specific structural dimensions. After optimization, the mass and deflection were reduced by 7.45% and 3.08%, respectively, and the modal frequency was increased by 0.42%. These results confirm that the optimization improves the performance of the crossbeam structure. Cao et al. [5] developed a dynamic model for high-speed spindle-tool systems based on Timoshenko beam theory and Jones bearing modeling theory. Their cutting parameter optimization methodology, derived from spindle-process coupling analysis, was implemented in face milling operations of aluminum helicopter

gearbox housings. Through optimal selection of axial cutting depth and rotational speed, material removal efficiency increased by 275%. Liu et al. [6] established a multi-objective optimization architecture integrating parameter sensitivity evaluation with quadratic response surface methodology to holistically optimize saddle assembly mass, Z-directional displacement, and fundamental frequency. This approach generated optimized stiffener structural designs with reduced mass/displacement, elevated modal frequencies, and rationally allocated stiffener dimensions.

As a critical load-bearing and supporting component in CNC machine tools, the crossbeam interfaces with columns through base bolted joints and supports gantry assemblies via front-installed linear guideways. Its static-dynamic behavior directly governs machining accuracy. Enhancing the crossbeam's deformation resistance performance constitutes a key technical approach for advancing machining precision and overall machine tool performance.

2. STATIC-DYNAMIC CHARACTERISTICS ANALYSIS OF THE CROSSBEAM

2.1. Machining Center Configuration and Cutting Force Computation

Fig. 1 illustrates the fixed-gantry machining center investigated in this study.

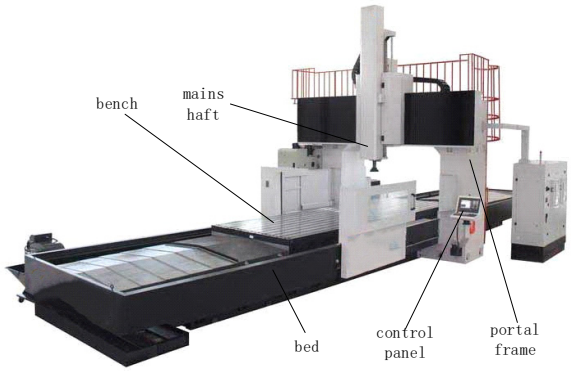

Fig 1. Fixed-Gantry Machining Center

Fig. 2 shows the spatial force analysis of the crossbeam. A coordinate system O-xyz is established with the center of the crossbeam guide rail as the origin. The x-axis corresponds to the movement direction of the worktable, the y-axis to the lengthwise direction of the crossbeam guide rail, and the z-axis to the vertical direction. G_0 represents the self-weight of the crossbeam, while G denotes the weight of the components mounted on the beam, F_0, F_f, F_{fN} are the components of the cutting force along the x, y, and z axes, respectively.

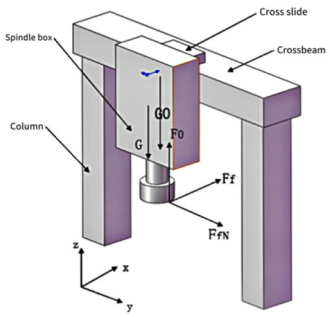

Fig 2. Spatial force analysis of the crossbeam.

Cutting force is the resistance exerted by the workpiece material against the tool during machining[7]. For machine tool design, the main cutting force along the movement direction of the worktable must be decomposed into three orthogonal components, as illustrated in Fig. 3.

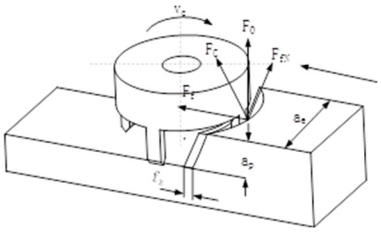

Fig 3. Cutting Force Components

Based on safety factor considerations, the calculated values of the force components are as follows: Fx = 6240 N, Fy = 8580 N, Fz = 14820 N.

2.2. Finite Element Model of the Crossbeam

The three-dimensional solid model of the crossbeam was constructed using SolidWorks, as shown in Fig. 4.

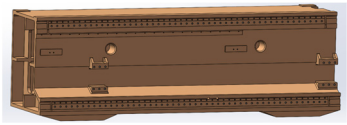

Fig 4. Three-dimensional solid model of the crossbeam

The selection of mesh size and element type significantly affects the accuracy of finite element analysis (FEA) results. For machine tool base components, the typical mesh size ranges from 15 mm to 30 mm. To achieve a balance between computational efficiency and result accuracy, mesh sizes were tested at 5 mm intervals within a range of 10 mm to 30 mm. Based on comparative analysis, a mesh size of 15 mm was determined to offer satisfactory accuracy and mesh quality. The mesh size under this setting is shown in Fig. 5.

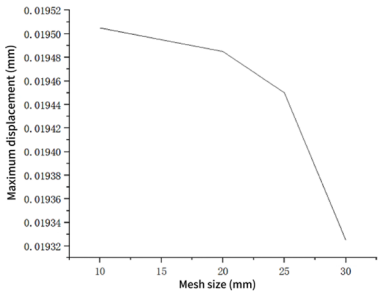

Fig 5. Deformation of the crossbeam under different mesh sizes

The final meshing of the crossbeam is illustrated in **Fig. 6**, with a mesh size of 15 mm, totaling 545,072 elements and 944,998 nodes.

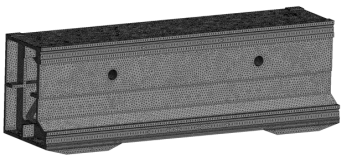

Fig 6. Finite element mesh of the crossbeam

2.3. Static Analysis of the Feed System

After completing material assignment, mesh generation, load application, and boundary condition setup, equivalent displacement and equivalent stress modules were inserted in the solver to conduct the simulation. The resulting stress contour and deformation contour of the crossbeam were obtained.

The deformation cloud diagram of the crossbeam is shown in **Fig. 7**, where the maximum deformation is 0.019483 mm, occurring near the center of the top surface of the beam. The stress distribution is illustrated in **Fig. 8**, where the maximum equivalent stress is 7.0687 MPa, located on the lower guide surface of the beam, close to the region in contact with the upper assembly components.

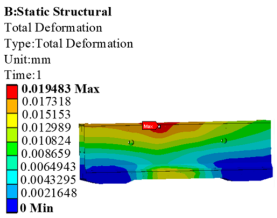

Fig 7. Deformation contour of the crossbeam

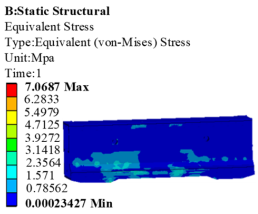

Fig 8. Equivalent stress contour of the crossbeam

For beams with both ends fixed, the maximum deformation typically appears at the midpoint. However, in the fixed-gantry machining center, the crossbeam is not perfectly symmetrical with respect to the central axis, and the components attached to both ends of the crossbeam are different, resulting in an uneven mass distribution. To accurately determine the location of maximum deformation, multiple finite element analyses were conducted. In the middle section of the crossbeam, 1400 mm from each end, a 130 mm segment was studied with measurement points set at 20 mm intervals, resulting in 21 static simulations in total. A polyline chart of the maximum deformation of the crossbeam under different positions of the upper components along the guide rail is shown in **Fig. 9**.

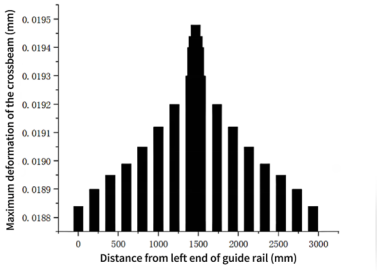

Fig 9. Deformation of the crossbeam under different positions of the upper assembly

When the upper assembly is positioned at the center of the crossbeam, the maximum deformation occurs. The peak deformation is 0.019483 mm. Therefore, the configuration with the upper assembly located at the center of the beam is selected as the extreme working condition for subsequent analysis.

3. DYNAMIC CHARACTERISTICS ANALYSIS OF THE CROSSBEAM

In this study, the dynamic characteristics of the crossbeam in a fixed-gantry machining center are analyzed to obtain key parameters such as natural frequencies, mode shapes, and response amplitudes. These data serve as the basis for the subsequent topology optimization design of the machining center.

3.1. Modeling of Crossbeam Joints

An accurate analysis of the dynamic behavior of the crossbeam structure depends critically on the modeling of its joints. In this study, the joint regions of the crossbeam are modeled using the method proposed by Yoshimura Mitsutaka. The relationship between joint stiffness, damping, and average contact pressure is shown in **Fig. 10**. By calculating the average contact pressure on the mating surfaces, the equivalent spring stiffness per unit area in both the shear and normal directions, as well as the equivalent viscous damping coefficients and the stiffness-to-damping ratio, can be derived. These values are then used to calculate the equivalent damping ratio and equivalent spring stiffness. These equivalent parameters are defined within the modal analysis module of ANSYS Workbench to accurately represent the contact conditions at the crossbeam joints.

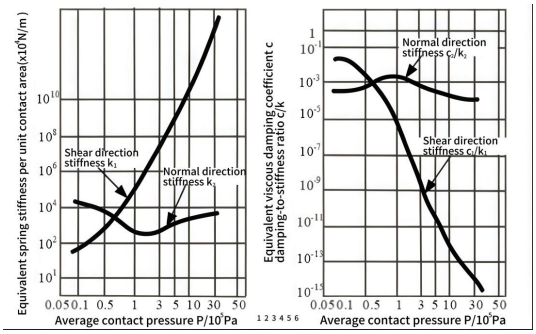

Fig 10. Relationship between stiffness, damping, and average contact pressure

The crossbeam has two contact interfaces: 1. The lower surfaces on both sides of the crossbeam are bolted to the top surfaces of the columns. 2. The front face of the crossbeam is bolted to the upper and lower guide rails. A tightening torque is applied using a 0.2 m wrench with a force of 100 N. According to Eq. (1) and Eq. (2), the corresponding preload force of the bolts can be calculated as follows:

$$T=0.2QD \tag{1}$$

$$T=LN \tag{2}$$

Q represents the preload force, T is the tightening torque, D is the bolt diameter, L is the lever arm length, and N is the applied force on the wrench. The tightening torque is calculated to be 19.6 $N{\cdot}m$ Each side of the crossbeam is connected to the corresponding column by eight M20 bolts. Assuming the preload force of each bolt at the crossbeam–column interface is Q_1, then Q_1=4900 N. The total contact force on this interface is given by Eq. (3):

$$F=n_1{\cdot}Q_1=39200N \tag{3}$$

The contact area at this interface is 180,762.04 mm². By uniformly distributing the total preload force over this area, the average contact pressure is calculated as: P1=2.169×105 N/m2.

The connection between the crossbeam and the guide rails is secured by 49 M14 bolts on each side. With a tightening torque of 19.6 N· m, the preload force for each bolt is Q_2=6125N. The total preload force applied to this contact interface is given by Eq. (4):

$$F=n_2{\cdot}Q_2=300125N \tag{4}$$

The stiffness and damping coefficients of the contact interface in the shear and normal directions are as follows: $K_1=1.4476\times10^{10}$ N/m, $K_2=8.6856\times10^{2}$ N/m, $C_1=1.4476\times10^{-3}$ N·s/m, $C_2=6.9486$ N·s/m.

3.2. Modal Analysis Results

The mesh and relevant settings were transferred from the static structural module to the modal analysis module. The computed stiffness and damping values at the contact interfaces were then applied for the simulation. The first six natural modes of the crossbeam were obtained through the modal analysis. The results are shown in **Fig. 11**.

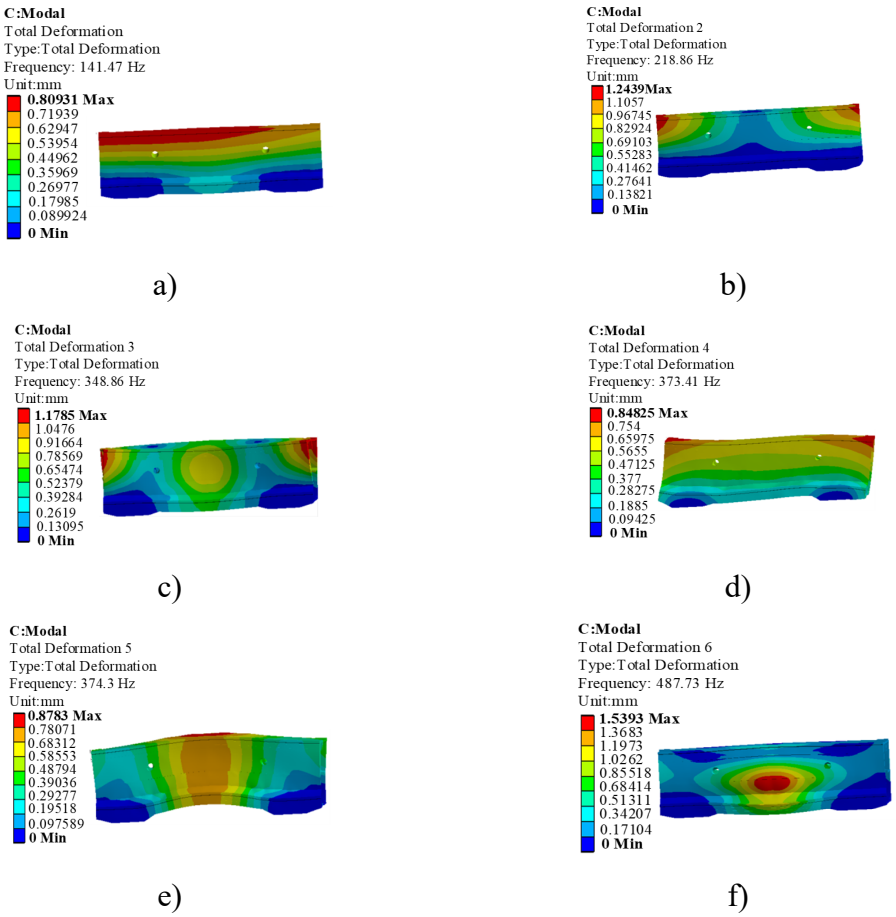

Fig 11. First six natural vibration modes of the crossbeam

Caption: (a) 1st mode; (b) 2nd mode; (c) 3rd mode; (d) 4th mode; (e) 5th mode; (f) 6th mode

The first six natural frequencies of the crossbeam are summarized in Table 1.

Table 1. Natural frequencies of the crossbeam

Mode	Frequency (Hz)	Mode	Frequency (Hz)
1	141.47	4	373.41
2	218.86	5	374.3
3	348.86	6	487.73

To compare the differences between joint modeling and the conventional fixed-constraint method, a second modal analysis was performed by applying fixed constraints at the interfaces between the crossbeam and the columns. The first six natural frequencies obtained under both constraint conditions are summarized in **Table 2**. The vibration modes of the crossbeam remain the same under both constraint schemes, and the values of the first six natural frequencies are generally close.

However, the frequencies under the fixed constraint are slightly higher than those under the spring–damper constraint, with the difference accounting for approximately 2% of the fixed-constraint values. The spring–damper constraint approach results in a slightly reduced overall stiffness of the crossbeam, which better reflects the actual boundary conditions of the structure.

Table 2. Modal frequencies of the crossbeam under different constraint conditions

	1	2	3	4	5	6
Spring–Damper Constraint (Hz)	141.47	218.86	348.86	373.41	374.3	487.73
Fixed Constraint (Hz)	144.65	225.4	354.79	381.99	381.41	499.92
Difference (Hz)	3.18	6.54	5.93	8.59	7.11	12.19
Difference Ratio (%)	2.2%	2.9%	1.7%	2.2%	1.8%	2.4%

During the design of the crossbeam, it is critical to ensure that the low-order natural frequencies are sufficiently separated from the excitation frequencies of the machine tool. If the excitation frequency is close to the natural frequency of the crossbeam, resonance may occur, resulting in a significant increase in vibration amplitude.Under the operating conditions of this study, the excitation frequency of the machine tool is $f=Zn/60=35.3Hz$. This frequency is well separated from the natural frequencies of the crossbeam, indicating that the structure is dynamically safe.

3.3. Harmonic Response Analysis of the Crossbeam

Harmonic response analysis is a technique used to determine the steady-state response of a linear structure subjected to loads that vary sinusoidally with time. This analysis provides the relationship between vibration amplitude and excitation frequency[8]. While modal analysis yields only the relative displacements of the system at its natural frequencies, harmonic response analysis offers a more intuitive evaluation of the vibration resistance of the structure under dynamic loading. Therefore, it is necessary to perform harmonic response analysis to assess the crossbeam's dynamic performance more comprehensively.

3.3.1. Harmonic Response Analysis Method

Harmonic response analysis was conducted using the ANSYS Workbench platform. The results from the modal analysis were transferred to the harmonic response module, with the data flow and module coupling shown in Fig. 12. In the harmonic response setup, external excitation forces were applied according to actual operating conditions. The frequency sweep was set from 0 to 600 Hz, with 100 frequency points analyzed in total, corresponding to an interval of 6 Hz.

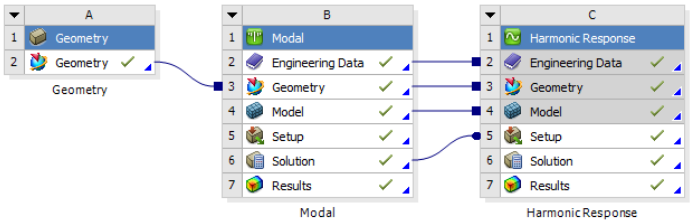

Fig 12. Workflow relationship between modal analysis and harmonic response analysis

Since the crossbeam is mechanically coupled with the upper components, its vibration behavior directly affects the relative motion between the tool and the workpiece surface through the spindle system. This, in turn, influences the machining accuracy and surface quality of the final parts. Therefore, the harmonic response curve was extracted at the center of the guide rail surface where the crossbeam interfaces with the upper components.

3.3.2. Harmonic Response Analysis Results

The amplitude–frequency response curves in the X, Y, and Z directions at the centroid of the guide rail surface—where the crossbeam interfaces with the upper components—are shown in **Fig. 13**.

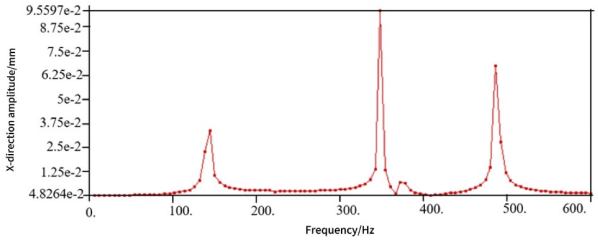

a)

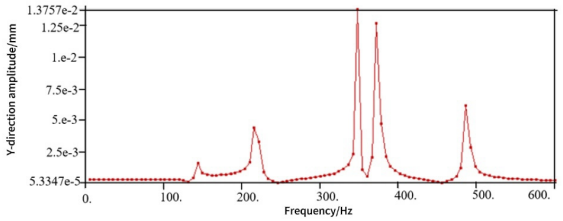

b)

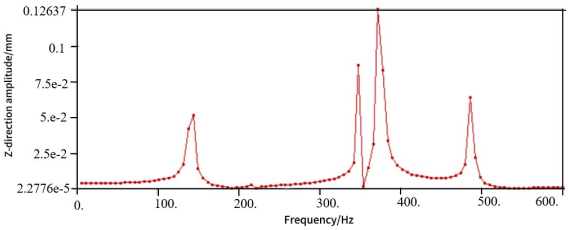

c)

Fig 13. Frequency response curves at the center of the crossbeam guide rail

Caption: (a) X-axis; (b) Y-axis; (c) Z-axis

By comparing the amplitude values, it can be observed that the order of frequency response amplitudes along the three coordinate directions is: Z-axis > X-axis > Y-axis. This result is consistent with the findings from the modal analysis, thereby validating its accuracy.

4. CROSSBEAM OPTIMIZATION DESIGN

The results of the static and dynamic analyses indicate that the crossbeam exhibits good mechanical performance [9]. However, the material distribution within the crossbeam is often not fully optimized, resulting in excessive structural mass. To address the issue of material redundancy in the crossbeam, a dual optimization strategy is proposed that combines topology optimization with bionic design. First, topology optimization is employed to determine the optimal material distribution. Then, inspired by the efficient evolutionary structure of a turtle shell, a bionic approach is adopted to optimize the rib layout.

This strategy not only ensures the crossbeam's dynamic and static performance, but also achieves structural lightweighting and rational load-bearing configuration, reflecting the integration of engineering optimization and natural design principles.

4.1. Topology Optimization of the Crossbeam

In this study, the density-based method is used for topology optimization. There are two commonly used interpolation functions to define material density thresholds in this method: the SIMP model and the RAMP model. Compared with SIMP, the RAMP model is more complex and less commonly applied. Therefore, the SIMP (Solid Isotropic Material with Penalization) model is adopted for the topology optimization of the crossbeam[10].

In the SIMP model, the material density of each finite element varies within the range [0,1], depending on the working conditions and loading state. After optimization, elements with densities close to 0 are typically removed, while elements with densities close to 1 are retained[11]. The **penalization factor** plays a key role in controlling the distribution of intermediate-density elements. A higher penalization factor increases the penalty on intermediate densities, driving the solution toward a clearer 0–1 distribution and resulting in a more distinct and interpretable topology for the crossbeam.

The results of the static and dynamic analyses indicate that the crossbeam performs well in terms of mechanical characteristics, yet still offers considerable potential for structural optimization. In this study, the **mass retention ratio** of the crossbeam is set within the range [0.5,0.6], with an increment of 0.01. A topology optimization is conducted for each step, resulting in 11 optimization iterations in total. By comparing the topology optimization results under different mass retention ratios, the evolution of material distribution within the crossbeam can be observed. As the mass retention ratio increases, additional material gradually accumulates around the central region of the crossbeam and the two vertex areas above the front face. In contrast, other regions show relatively minor changes. These two regions are identified as areas with significant material redundancy.

The topology optimization results for mass retention ratios of 50% and 60% are shown in Fig. 14.

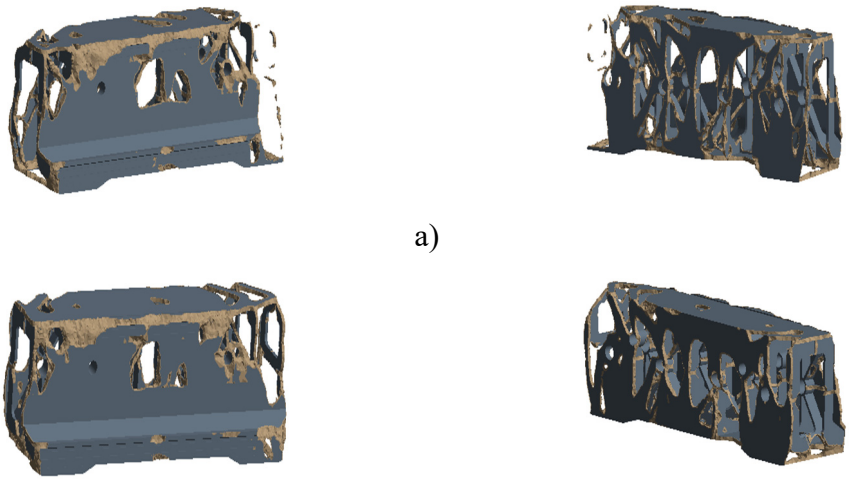

a)

b)

Fig 14. Topology optimization results of the crossbeam

Caption: (a) Mass retention ratio: 50%; (b) Mass retention ratio: 60%

To further evaluate the material utilization across different regions of the crossbeam and fully explore its optimization potential, an additional set of topology optimizations was performed using a **solid (non-hollow) crossbeam**. A static structural analysis was first conducted on the solid crossbeam, using the same boundary conditions and loading settings as before.

The results of this static analysis were then transferred to the topology optimization module. As in the previous case, the mass retention ratio was set within the range of 50% to 60%, with a total of 11 iterations conducted. All other simulation settings remained unchanged. The topology optimization

results for the solid crossbeam are shown in **Fig. 15**. Similar to the original crossbeam, material redundancy is again observed in the **central region** and in the **two vertex areas above the front face**, indicating that these areas have considerable potential for structural refinement and weight reduction.

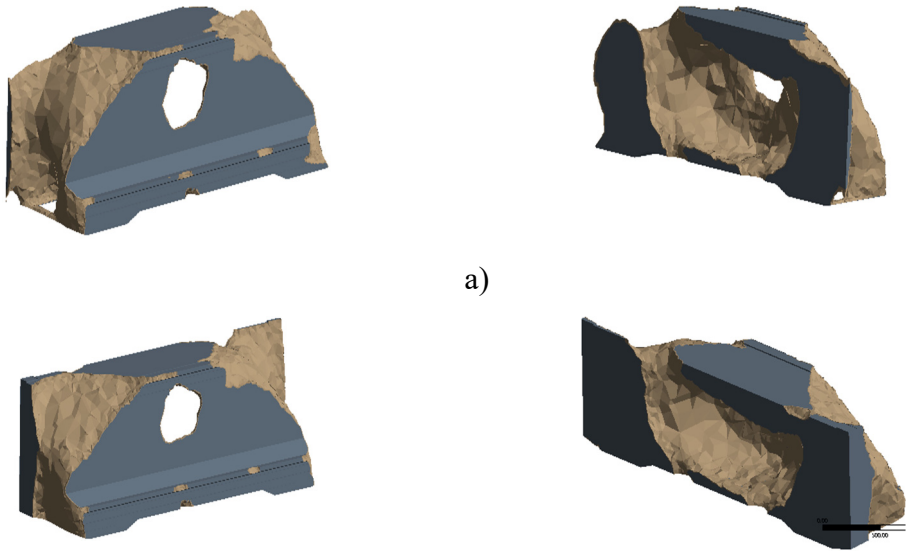

a)

b)

Fig 15. Topology optimization results of the solid crossbeam

Caption: (a) Mass retention ratio: 50%; (b) Mass retention ratio: 60%

By comparing the topology optimization results of the original and solid crossbeam models, it is evident that the crossbeam contains significant material redundancy and has potential for further optimization. As the mass retention ratio decreases from 60% to 50%, material removal becomes more pronounced in the central internal region of the crossbeam and around the two vertex areas above the front face. In contrast, material removal in other regions remains relatively unchanged.

Based on the topology-optimized model and taking manufacturability into account, structural design efforts are focused on the internal configuration of the crossbeam, specifically including the design of internal stiffening ribs and cut-outs on the end faces. The delicate structures of living things provide design solutions and design prototypes for human engineering problems. Biological evolution always evolves towards the most material-, force-, and energy-efficient direction, and their structures are then constantly changing to meet evolutionary needs and to be more adaptive to the environment[12]. Examples include the veins of leaves[13], the streamlined structure of fish[14], and the bamboo joints of bamboo[15].

4.2. Bionic Optimization of the Crossbeam

The results of topology optimization provide valuable guidance for structural redesign of the crossbeam. However, the internal rib layout still allows for multiple design possibilities. To explore a more rational and efficient rib configuration, inspiration can be drawn from **biological structures found in nature**.

4.2.1. Selection of Bionic Prototype

The turtle shell is a well-known example of a natural structure with high mechanical performance. When moving on land or swimming in water, a turtle can retract its limbs into its shell to protect itself from external threats. Even when subjected to vertical pressure, the rigid shell provides excellent protection against external damage.

The high load-bearing capacity of the turtle shell is closely related to its unique structural configuration. As shown in Fig. 16, the shell consists of a flat plastron on the bottom and a domed

carapace on the top. Internally, the shell contains the vertebrae, sternum, and ribs, which are directly connected to the carapace. Moreover, at the four corners of the shell, bone-like supporting structures are present to enhance mechanical strength.

Fig 16. Structural configuration of the turtle shell

Bionic design is not a simple process of imitation. The selected biological prototype must share a certain degree of structural or functional similarity with the engineering object of study in order to serve as a meaningful reference[16].

4.2.2. Similarity Evaluation

Let the similarity between the bionic prototype and the engineering object be denoted by Q, where $Q \in [0,1]$. The closer Q is to 1, the greater the similarity, indicating a higher feasibility and effectiveness of bionic design. Conversely, if Q approaches 0, the similarity is low and the prototype is considered unsuitable for bionic optimization.

In the process of similarity evaluation, each aspect of comparison between the bionic prototype and the target structure is referred to as a feature. All features are treated as similarity elements, and the overall similarity Q is computed by evaluating the collective similarity across these features.

The similarity coefficient Q is calculated according to Eq. (5):

$$Q=\sum_{i=1}^{n}(\beta_1 q(u_1)+\beta_2 q(u_2)+\cdots+\beta_n q(u_n))=\sum_{i=1}^{n}\beta_i q(u_i) \tag{5}$$

In the equation, Q represents the overall similarity coefficient, n is the total number of features to be evaluated, and β_i is the weight coefficient assigned to the i-th feature, where $0<\beta_i<1$ and $\sum_{i=1}^{n}\beta_i=1$. The variable u denotes a similarity element, and $q(u_i)$ indicates the similarity score of the element u_i.

To evaluate the degree of similarity between the bionic prototype and the engineering object, all relevant features are assessed to form a set of similarity elements: $U=\{u_1,u_2,\cdots u_n\}$

In this set, u_{ij} denotes the relative importance of the i-th feature compared to the j-th feature. By organizing these pairwise comparisons, a **judgment matrix** can be established, as shown in Eq. (6).

$$P=\begin{bmatrix} u_{11} & u_{12} & \cdots & u_{1j} & \cdots & u_{1n} \\ u_{21} & u_{22} & \cdots & u_{2j} & \cdots & u_{2n} \\ \cdots & \cdots & & \cdots & & \cdots \\ u_{i1} & u_{i2} & \cdots & ui_j & \cdots & u_{in} \\ \cdots & \cdots & & \cdots & & \cdots \\ u_{n1} & u_{n2} & \cdots & u_{nj} & \cdots & u_{nn} \end{bmatrix} \tag{6}$$

In the judgment matrix, the elements satisfy the following conditions: $u_{ij}>0$, $u_{ii}=1, u_{ij}=u_{ji}^{-1}, i=(1,2,\cdots n), j=(1,2,\cdots n)$ The values of u_{ij} are assigned based on a standard reference scale (see Table 3). The **weight coefficient** β_i is derived from the **eigenvector** of the judgment matrix P.

Table 3. Fundamental scale for pairwise comparison in AHP

Value	Relative importance of factor A compared to factor B
1	A and B are equally important
3	A is slightly more important than B
5	A is significantly more important than B
7	A is strongly more important than B
9	A is extremely more important than B
2, 4, 6, 8	Intermediate values between adjacent judgments
Reciprocal	If A is assigned a value relative to B, then B is assigned the reciprocal value relative to A

Once the judgment matrix has been constructed, it must be evaluated to ensure its correctness and rationality. For this purpose, the Consistency Ratio (*C.R.*) is introduced. The calculation is shown in Eq. (7):

$$C.R.=\frac{C.I.}{R.I.} \tag{7}$$

where *C.I.* denotes the Consistency Index, and *R.I.* represents the Random Index, which is the average consistency index of randomly generated matrices of the same order.

The Consistency Index (*C.I.*) is calculated using Eq. (8):

$$C.I.=\frac{\lambda_{max-n}}{n\text{-}1} \tag{8}$$

In this equation,λ_{max}represents the **maximum eigenvalue** of the judgment matrix, and nnn is the **order of the matrix**.

The detailed computation of λ_{max} is given in Eq. (9):

$$\lambda_{max}=\frac{1}{n}\sum_{i=1}^{n}\frac{\sum_{i=1}^{n}u_{ij}\beta_j}{\beta_i} \tag{9}$$

In addition, the values of the **Random Index (R.I.)** can be referenced from **Table 4**:

Table 4. Reference values for the Random Index (R.I.)

n	2	3	4	5	6	7	8
R. I.	0	0.5149	0.8931	1.1185	1.2494	1.3450	1.4200

Once the **Consistency Ratio (C.R.)** is calculated, it is used to evaluate the consistency of the judgment matrix *P*. If *C.R.*<0.1, the matrix *P* is considered **consistent and acceptable.** If *C.R.*>=0.1, the matrix is considered **inconsistent and unreliable**, and the judgment matrix must be reconstructed and re-evaluated.

The similarity of individual similarity elements $q(u_i)$ is calculated using Eq. (10):

$$q(u_i)=\frac{m}{\mathrm{h}+p-n}\sum_{j=1}^{m}f_j d_{ij} \tag{10}$$

In the equations: *h* and *p* represent the total number of similarity features, h_j denotes the weight of the *j*-th feature, *m* is the number of shared similarity features, and d_{ij} is the **feature value ratio coefficient**.

The ratio coefficient d_{ij} is calculated using Eq. (11):

$$d_{ij}=\frac{min\left(U_j(C_i),U_j(D_i)\right)}{max\left(U_j(C_i),U_j(D_i)\right)} \tag{11}$$

In this context, $\left(U_j(C_i),U_j(D_i)\right)$ represent the **equivalent feature values** of fuzzy similarity systems C and D under the j-th feature. The operators min and max indicate the minimum and maximum values of the equivalent feature values, respectively.

Through the computational procedure described above, the similarity value between the bionic prototype and the engineering object can be determined. Assuming the similarity between the crossbeam of the fixed-gantry machining center and the turtle shell is denoted by Q, and the two share four similarity features—**structure**, **function**, **load**, and **constraint**—the corresponding judgment matrix P is shown in Eq. (12):

$$P=\begin{bmatrix} 1 & 3 & 3 & 2 \\ \frac{1}{3} & 1 & 1 & 2 \\ \frac{1}{3} & 1 & 1 & 2 \\ \frac{1}{2} & \frac{1}{2} & \frac{1}{2} & 1 \end{bmatrix} \tag{12}$$

Based on the judgment matrix P, the eigenvector is calculated as: $\alpha=(0.45,0.2,0.2,0.15)^T$

The maximum eigenvalue is λ_{max}, and the corresponding weight vector is:

$$\beta=(0.45,0.2,0.2,0.15)^T$$

The consistency index is calculated as:

$$C.I.=\frac{\lambda_{max}}{n\text{-}1}\frac{4.2175\text{-}4}{4\text{-}1}$$

Given that the random index $R.L.$=0.8931, the consistency ratio is:

$$C.L.=0.0812<0.1$$

Thus, the judgment matrix is considered consistent and acceptable. The similarity scores of individual similarity elements are given as:

$$q=(0.8,0.6,0.8,0.45)$$

Therefore, the overall structural similarity Q between the turtle shell and the crossbeam is calculated as:

$$Q=0.8\times0.45+0.6\times0.2+0.8\times0.2+0.45\times0.15=0.7075$$

Since the similarity score is relatively high, it indicates that the structural characteristics of the turtle shell can serve as a valid reference for the bionic design of the crossbeam.

4.2.3. Structural Remodeling of the Crossbeam

The topology optimization results reveal that material redundancy in the crossbeam is primarily concentrated in the central region. This observation, combined with insights from the bionic design inspired by the turtle shell, serves as the basis for the structural redesign of the crossbeam.

The turtle shell features a domed upper structure and a relatively flat lower part. Accordingly, the crossbeam is divided into upper and lower regions for targeted structural design. The upper section is reinforced with arched rib structures, while the lower section incorporates vertical ribs for direct support.

Given the significant material redundancy in the central portion of the crossbeam, through-holes are introduced in this region to reduce mass. The central through-hole is designed to be slightly larger

than the adjacent side holes, and no openings are made in the two arched sections on either end. A sectional view of the preliminarily designed crossbeam model (Model I) is shown in Fig. 17.

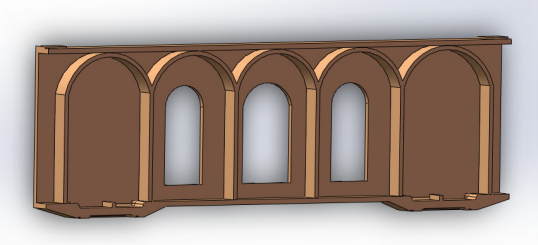

Fig 17. Cross-sectional view of the bionic crossbeam (Model I)

Considering that the left and right ends of the crossbeam exhibit minimal material redundancy, as indicated by the small amount of material removed in the topology optimization results, the material utilization in these regions is relatively high. Based on this observation, an improved bionic crossbeam design—Model II—is proposed. In this model, an X-shaped rib structure is added beneath each of the two arched sections at both ends of the beam. The sectional view of the redesigned crossbeam is shown in Fig. 18.

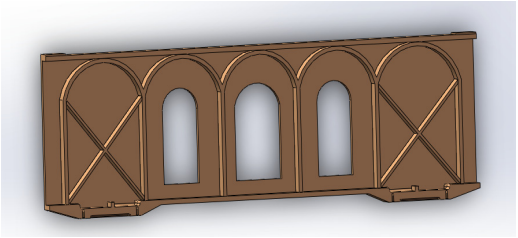

Fig 18. Cross-sectional view of the bionic crossbeam (Model II)

Finite element simulations were conducted for both bionic crossbeam models under actual working conditions. Loads and boundary conditions were applied consistent with those used in the previous static analysis. The resulting maximum deformation cloud diagrams for the two crossbeams are shown in Fig. 19.

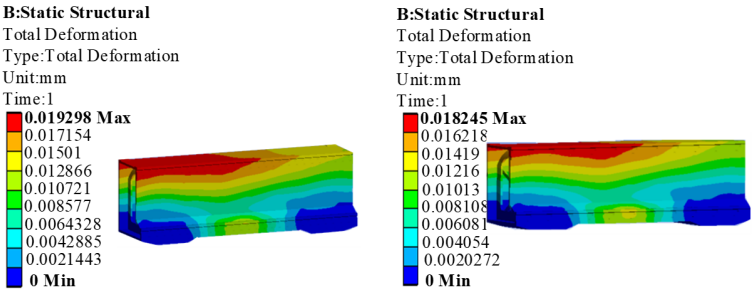

Fig 19. Maximum deformation of crossbeam Models I and II

Table 5. Comparison of crossbeam performance parameters before and after optimization

Parameter	Original Crossbeam	Optimized Crossbeam (Model II)	Change Rate (%)
Mass (kg)	4390.35	3750.35	14.58%
Maximum deformation (mm)	0.019483	0.018425	5.43%
Maximum stress (MPa)	7.0687	7.8573	11.2%
First-order natural frequency (Hz)	141.47	145.51	2.9%

The deformation results indicate that the maximum displacement of Model I is 0.019298 mm, whereas that of Model II is 0.018245 mm. The smaller deformation in Model II suggests that it exhibits better resistance to structural deflection compared to Model I. A comprehensive comparison of key performance indicators—including maximum stress, the first six natural frequencies, and the amplitude responses at the guide rail center in all three directions—shows that Model II outperforms Model I across all metrics. Therefore, Model II is selected as the optimized design for further study and refinement. A detailed comparison of the structural performance between the original crossbeam and the optimized Model II is presented in Table 5.

By comparing the original crossbeam with the optimized version, it is observed that the optimized crossbeam achieves a 14.58% reduction in mass, a 5.43% decrease in maximum deformation, and a 2.9% increase in the first-order natural frequency. However, the maximum stress increases by 11.2%.

This analysis indicates that the addition of reinforcing ribs at both ends of the crossbeam significantly improves its overall performance compared to the unreinforced design. The internal rib structure and layout within the crossbeam have a substantial impact on its mechanical behavior.

To further explore this effect, alternative rib configurations are proposed for the arched sections on both sides of the crossbeam. In addition to the existing X-shaped ribs, three new reinforcement schemes are introduced: star-shaped, grid-shaped, and diamond-shaped ribs. The corresponding crossbeam models are illustrated in Fig. 20.

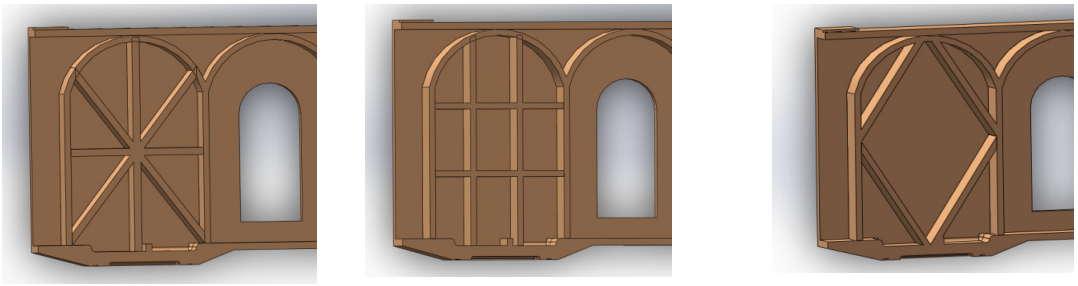

(a) Star-shaped ribs (b) Grid-shaped ribs (c) Diamond-shaped ribs

Fig 20. Cross-sectional views of crossbeams with different rib configurations

A new set of finite element simulations was conducted for the three redesigned crossbeam models with different rib configurations. The key performance parameters of each design are summarized in Table 6.

Table 6. Performance comparison of crossbeam models before and after optimization

Parameter	Star-Shaped Rib	Grid-Shaped Rib	Diamond-Shaped Rib
Mass (kg)	3881.25	3915.89	3780.57(√)
Maximum deformation (mm)	0.015976(√)	0.016652	0.018683
Maximum stress (MPa)	6.7153(√)	6.9541	7.1538
First-order natural frequency (Hz)	152.24(√)	148.47	143.62

Based on the comparison under identical simulation settings, the star-shaped rib design demonstrates superior overall performance. Therefore, the star-shaped configuration is selected as the final rib structure for the crossbeam.

The stress distribution and deformation contour of the star-shaped crossbeam are shown in Fig. 21. It can be observed that the maximum deformation occurs at the top center of the crossbeam, near the front face, with a deformation magnitude of 0.015976 mm. The maximum stress appears near the lower guide surface at the front face, with a stress value of 6.7153 MPa.

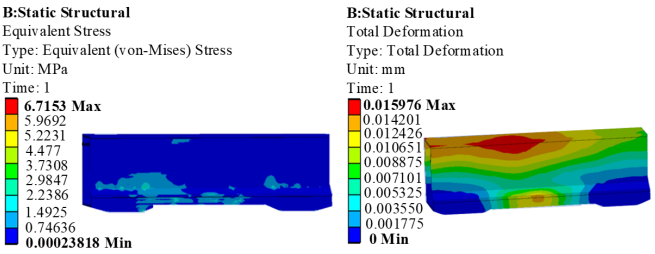

Fig 21. Stress and deformation contours of the star-shaped rib crossbeam

The performance comparison between the star-shaped rib crossbeam and the original crossbeam is presented in Table 7. The optimized design shows improvements across all evaluated parameters, including mass, maximum deformation, maximum stress, and first-order natural frequency.

Specifically, the mass of the crossbeam was reduced by 11.59%, the maximum deformation decreased by 18%, and the maximum stress was reduced by 5%. Additionally, the first-order natural frequency increased significantly by 20.3%, indicating a substantial enhancement in the dynamic performance of the structure.

Table 7. Comparison of performance parameters between the original and star-shaped crossbeam design

Parameter	Star-Shaped Rib	Grid-Shaped Rib	Diamond-Shaped Rib
Mass (kg)	4390.35	3881.25	-11.59%
Maximum deformation (mm)	0.019483	0.015976	-18%
Maximum stress (MPa)	7.0687	6.7153	-5%
First-order natural frequency (Hz)	141.47	152.24	+7.6%

Based on the results of topology optimization, a bionic design was applied to the crossbeam structure. Among the five crossbeam configurations studied, the one featuring a domed central section with through-holes and star-shaped reinforcing ribs inside the arched sections at both ends exhibited the best overall performance.

5. CONCLUSION

This study investigated the static and dynamic characteristics as well as the structural optimization of the crossbeam in a fixed-gantry machining center. Under loading conditions, the maximum deformation of the crossbeam was 0.019483 mm, occurring at the top center, while the maximum equivalent stress was 7.0687 MPa, concentrated at the interface between the lower guide rail and the crossbeam—both within acceptable limits for stiffness and strength.

The dynamic characteristics were analyzed using a joint modeling method based on Yoshimura's approach, yielding the first six natural frequencies in the range of 141.47 to 487.73 Hz. These results were validated by harmonic response analysis, which showed that the vibration amplitudes at the center of the guide rail followed the order: Z-axis > X-axis > Y-axis, confirming the accuracy of the modal analysis.

A novel crossbeam structure was then proposed by combining topology optimization (with mass retention ratios ranging from 50% to 60%) and bionic design (with a structural similarity score of 0.7075 to a turtle shell). The final design features a domed central section with through-holes and star-shaped ribs at both ends. Compared to the original design, the optimized crossbeam demonstrated significant improvements in static and dynamic performance, more efficient material distribution, and a substantial reduction in structural redundancy.

CONFLICT OF INTEREST

The authors declare that they have no known competing financial interests or personal relationships that could have appeared to influence the work reported in this paper.

DATA AVAILABILITY STATEMENT

The datasets generated and/or analyzed during the current study are available from the corresponding author upon reasonable request.

REFERENCES

[1] Liu S H, Du Y B, Lin M. Study on lightweight structural optimization design system for gantry machine tool. *Concurrent Engineering-Research and Applications*, 2019, 27(2): 170-185.

[2] Ahmed F, Ko T J, Jongmin L, et al. Tool Geometry Optimization of a Ball End Mill based on Finite Element Simulation of Machining the Tool Steel-AISI H13 using Grey Relational Method. *International Journal of Precision Engineering and Manufacturing*, 2021, 22(7): 1191-1203.

[3] Niu P, Cheng Q, Yang C, et al. Multi-objective Topology Optimization of Machine Tool Basic Part Column for Rib Layout. *Journal of Beijing University of Technology*, 2025, 51(3): 241-249.

[4] Li X G, Li C Q, Li P H, et al. Structural Design and Optimization of the Crossbeam of a Computer Numerical Controlled Milling-Machine Tool Using Sensitivity Theory and NSGA-II Algorithm. *International Journal of Precision Engineering and Manufacturing*, 2021, 22(2): 287-300.

[5] Cao H, Chen X, He Z. Modeling of Spindle-process Interaction and Cutting Parameters Optimization in High-speed Milling. *Chinese Journal of Mechanical Engineering*, 2013, 49(5): 161-166.

[6] Liu K, Liao Y, Tan Z, et al. Optimization of process parameters of five-axis machine tool's cross slide based on response surface method. *Journal of Machine Design*, 2025, 42(3): 113-123.

[7] Wang M H, Gao L, Zheng Y H. An examination of the fundamental mechanics of cutting force coefficients. *International Journal of Machine Tools & Manufacture*, 2014, 78: 1-7.

[8] García-Martínez E, Molina-Yagüe A, Miguel V, et al. Harmonic-based-on analysis to discriminate different mechanical actions involved in the machining of hard-to-cut materials. *The International Journal of Advanced Manufacturing Technology*, 2024, 133(1): 335-349.

[9] Liu S H, Li Y, Liao Y L, et al. Structural optimization of the cross-beam of a gantry machine tool based on grey relational analysis. *Structural and Multidisciplinary Optimization*, 2014, 50(2): 297-311.

[10] Kim D, Lazarov B S, Surowiec T M, et al. A simple introduction to the SiMPL method for density-based topology optimization. *Structural Multidisciplinary Optimization*, 2025, 68(4): 1-17.

[11] Cheng D, Lu X, Sun X. Multi-objective topology optimization of column structure for vertical machining center. *Procedia CIRP*, 2018, 78: 279-284.

[12] Shen L, Ding X, Li T, et al. Structural dynamic design optimization and experimental verification of a machine tool. *The International Journal of Advanced Manufacturing Technology*, 2019, 104: 3773-3786.

[13] Tang S N, Zhu Y, Yuan S Q. Bionics-Inspired Structure Boosts Drag and Noise Reduction of Rotating Machinery. *Journal of Bionic Engineering*, 2023, 20(6): 2797-2813.

[14] Ji S Y, Mou Q Y, Li T, et al. The Novel Applications of Bionic Design Based on the Natural Structural Characteristics of Bamboo. *Forests*, 2024, 15(7).

[15] Yan S N, Li B T, Hong J. Bionic design and verification of high-precision machine tool structures. *International Journal of Advanced Manufacturing Technology*, 2015, 81(1-4): 73-85.

[16] Dickinson M H. Bionics: Biological insight into mechanical design. *Proceedings of the National Academy of Sciences*, 1999, 96(25): 14208-14209.